Cell Reports

Report

Heterogeneous MAC Initiator and Pore Structures in a Lipid Bilayer by Phase-Plate Cryo-electron Tomography

Graphical Abstract

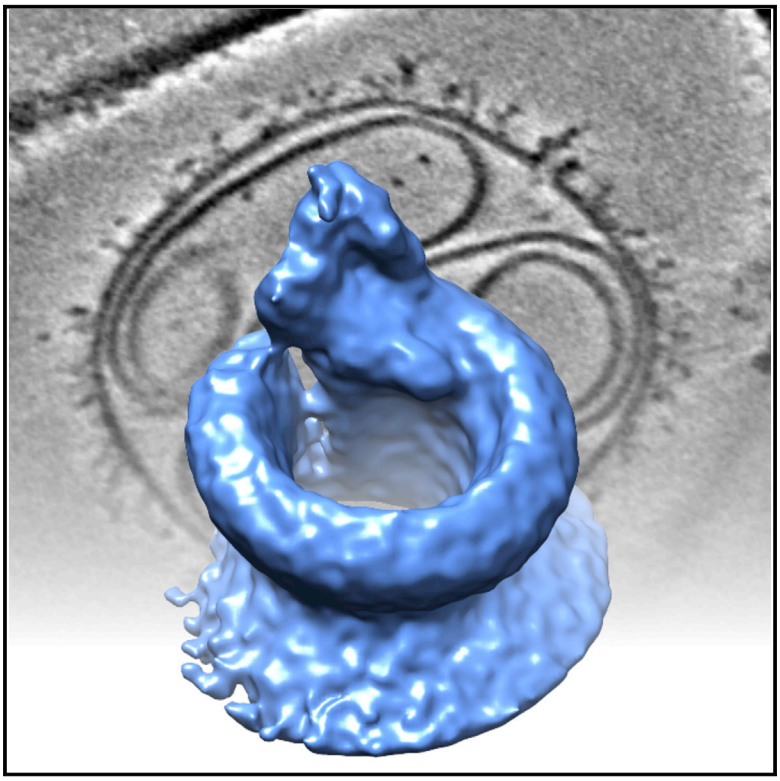

Authors

Thomas H. Sharp, Abraham J. Koster, Piet Gros

Correspondence

t.sharp@lumc.nl (T.H.S.), p.gros@uu.nl (P.G.)

In Brief

Immune defense by complement forms membrane attack complex pores in membranes. Using phase-plate cryo-electron tomography, Sharp et al. find heterogeneous oligomeric MAC structures in membranes. Subtomogram averaging of single pores at 2.3-nm resolution reveals a cone-shaped, twisted barrel that is incompletely closed.

Highlights

- MAC pores are cone shaped, twisted, and poorly sealed between C9 end and C5b-8 start
- Complement activation yields single and joined MAC pores in lipid membranes
- Oligomerization of three to four C5b-8 complexes causes ~3.5-nm pores in membranes
- Phase plates markedly increase interpretability of cryo-electron tomograms

Sharp et al., 2016, Cell Reports *15*, 1–8
April 5, 2016 ©2016 The Authors
http://dx.doi.org/10.1016/j.celrep.2016.03.002

Cell Reports
Report

OPEN ACCESS
CellPress

Heterogeneous MAC Initiator and Pore Structures in a Lipid Bilayer by Phase-Plate Cryo-electron Tomography

Thomas H. Sharp,[1,*] Abraham J. Koster,[1,2] and Piet Gros[3,*]
[1]Section Electron Microscopy, Department of Molecular Cell Biology, Leiden University Medical Center, 2300 RC Leiden, the Netherlands
[2]NeCEN, Gorlaeus Laboratories, Leiden University, 2333 CC Leiden, the Netherlands
[3]Crystal and Structural Chemistry, Bijvoet Center for Biomolecular Research and Department of Chemistry, Faculty of Science, Utrecht University, Padualaan 8, 3584 CH Utrecht, the Netherlands
*Correspondence: t.sharp@lumc.nl (T.H.S.), p.gros@uu.nl (P.G.)
http://dx.doi.org/10.1016/j.celrep.2016.03.002

SUMMARY

Pore formation in membranes is important for mammalian immune defense against invading bacteria. Induced by complement activation, the membrane attack complex (MAC) forms through sequential binding and membrane insertion of C5b6, C7, C8, and C9. Using cryo-electron tomography with a Volta phase plate and subtomogram averaging, we imaged C5b-7, C5b-8, and C5b-9 complexes and determined the C5b-9 pore structure in lipid bilayers. The in situ C5b-9 pore structure at 2.3-nm resolution reveals a 10- to 11.5-nm cone-shaped pore starting with C5b678 and multiple copies of C9 that is poorly closed, yielding a seam between C9 and C6 substituting for the shorter β strands in C6 and C7. However, large variations of composite pore complexes are apparent in subtomograms. Oligomerized initiator complexes C5b-7 and C5b-8 show stages of membrane binding, deformation, and perforation that yield ~3.5-nm-wide pores. These data indicate a dynamic process of pore formation that likely adapts to biological membranes under attack.

INTRODUCTION

Activation of the mammalian complement system induces formation of membrane attack complexes (MACs), yielding pores in membranes of invading microbes (see, e.g., Ricklin et al., 2010). MAC formation is critical for human defense against gram-negative bacteria of the *Neisseria* genus (Stephens et al., 2007). However, host cells are also vulnerable to MAC, as is apparent in paroxysmal nocturnal hemoglobinuria and atypical hemolytic uremic syndrome (Noris and Remuzzi, 2009; Parker, 2007). In recent years, awareness has grown that complement activation and MAC formation may impound on many disease pathogeneses that involve tissue maintenance, with various tissues affected, such as brain, heart, kidney, eyes, and teeth gums (see, e.g., Morgan and Harris, 2015; Ricklin et al., 2010).

MAC formation starts when C5 convertases cleave C5 into C5a and C5b (Müller-Eberhard, 1986). Upon production, C5b associates with C6, forming the soluble C5b6 complex (Cooper and Müller-Eberhard, 1970). Addition of C7 generates C5b67, denoted as C5b-7, which adheres to membranes (DiScipio et al., 1988; Preissner et al., 1985). Association of the heterotrimeric C8αβγ yields C5b-8, which forms small pores with a 0.9-nm diameter and, as time progresses, generates 3-nm pores (Ramm et al., 1982; Zalman and Müller-Eberhard, 1990). In normal human sera (NHS), C5b-9 creates ~10-nm pores (Tschopp, 1984). Negative-stain electron microscopy studies in the 1980s provided low-resolution images of C5b-7 (DiScipio et al., 1988; Preissner et al., 1985), C5b-8 (Bhakdi and Tranum-Jensen, 1984; Podack et al., 1982), and C5b-9 (Tschopp, 1984). Crystal structures of C5 (Fredslund et al., 2008), C6 (Aleshin et al., 2012b), and C8αβγ (Lovelace et al., 2011) and the first MAC-initiating complex, C5b6 (Aleshin et al., 2012a; Hadders et al., 2012), gave insights into structural details. Structures of MAC-perforin (MACPF) domains of C8α (Hadders et al., 2007) and Plu-MACPF from *P. luminescens* (Rosado et al., 2007) suggested a mechanistic resemblance to bacterial cholesterol-dependent cytolysins (CDCs), in which loosely folded α helices rearrange into transmembrane β-hairpins that extend from the kinked β strands, forming a β-barrel pore (Shatursky et al., 1999; Shepard et al., 1998). For the CDC perfringolysin, formation of pre-pore complexes on top of the membrane before membrane perforation was observed (Hotze et al., 2001). In contrast, half- or hemi-pores were posited for MAC formation (Bhakdi and Tranum-Jensen, 1984) and recently proposed to exist for CDC pneumolysin (Sonnen et al., 2014). Atomic-force microscopy studies confirm formation of these seemingly unfavorable membrane structures for CDC suilysin in phosphatidylcholine:cholesterol membranes (Leung et al., 2014).

Advances in cryo-electron tomography (cryo-ET; Asano et al., 2016; Nogales and Scheres, 2015) facilitate reinvestigations of in situ MAC formation in lipid bilayers. We took advantage of a Volta phase plate (Danev et al., 2014) installed on a Titan Krios transmission electron microscope with a Falcon II direct electron detector. This setup significantly improves the contrast at low resolution, which markedly increases the interpretability of tomographic volumes collected in focus (Fukuda et al., 2015) and

This is an open access article under the CC BY-NC-ND license (http://creativecommons.org/licenses/by-nc-nd/4.0/).

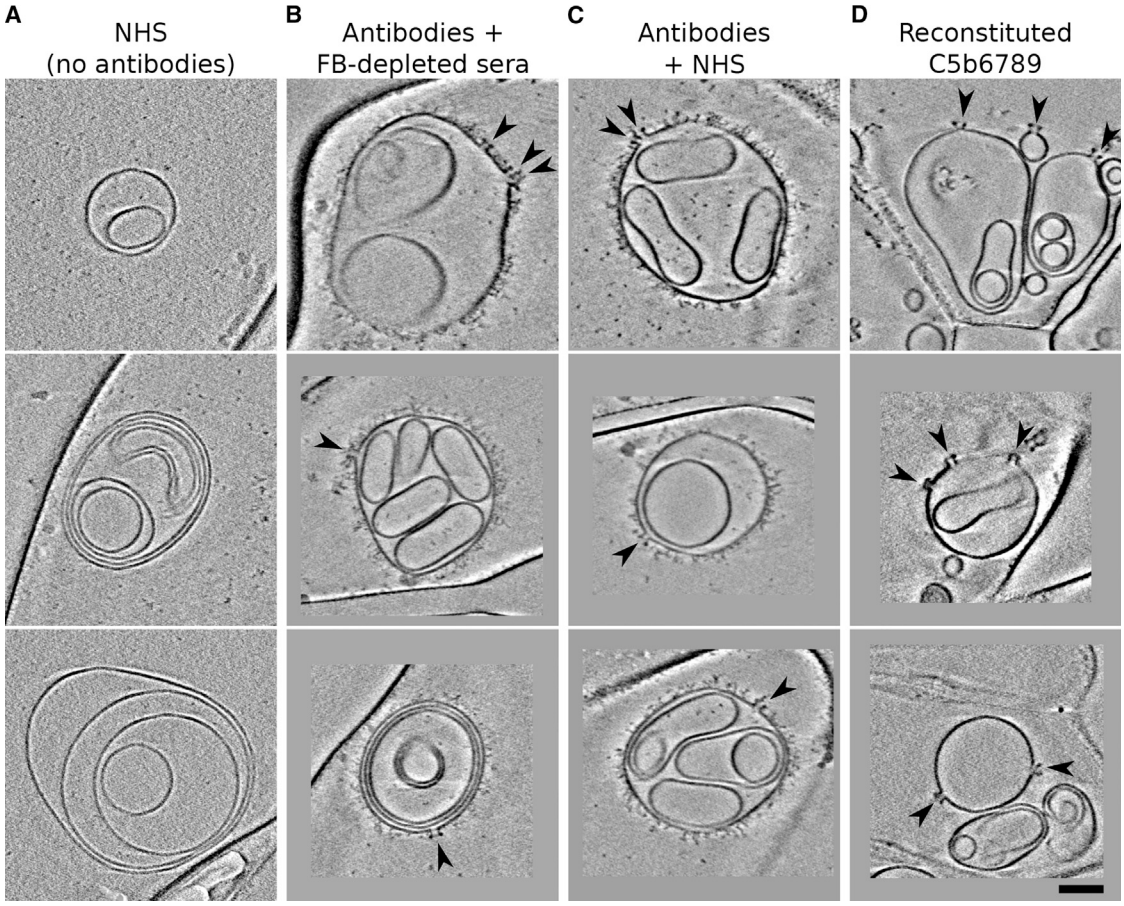

Figure 1. MAC Pores Form in Lipid Bilayers in the Presence of FB-Depleted Serum, NHS, and Reconstituted C5b6789
(A–D) Tomographic slices through multilamellar liposomes of ~200 nm in diameter in the presence of (A) NHS with no antibodies, (B) antibodies with FB-depleted sera, (C) antibodies with NHS, and (D) reconstituted C5b6789. Arrowheads indicate pores; several composite pores are observed (double arrows). Lacey-carbon support films are also visible. Scale bar represents 100 nm.

allows identification of heterogeneities in complex formation (Asano et al., 2015). Nevertheless, the resolution of single tilt-axis tomographic reconstructions is inherently limited by the tilt angles attainable, which are constrained to approximately ±60°, resulting in a missing wedge of data and anisotropic resolution. Particle averaging of subtomograms is necessary to fill in this missing wedge, thereby restoring isotropic resolution to the average (Briggs, 2013).

RESULTS AND DISCUSSION

For in situ cryo-ET imaging of MAC-pore formation, we used liposomes consisting of 45:5:50 mol % dimyristoylphosphatidylcholine (DMPC):dimyristoylphosphatidylglycerol (DMPG):cholesterol, with 0.5 mol % dinitrophenyl (DNP)-lipid haptens for antibody-induced complement activation. In the presence of anti-DNP complement-activating antibodies (Yamamoto et al., 1995), NHS yielded MAC-induced leakage of the DNP-carrying liposomes, with a 5-min lag phase and maximum leakage rates observed 15 min after induction (Figures S1A and S1B). Imaging of these liposomes in the presence of NHS without complement-activating antibodies showed bare membranes devoid of protein deposition and protein pore formation (Figure 1A). Thus, neither complement deposition nor protein binding occurred. Extensive complement deposition and MAC-pore formation were observed in experiments with complement-activating antibodies and either NHS or factor B (FB)-depleted sera (Figures 1B and 1C). When using FB-depleted sera, similar MAC pores are formed, indicating that our data are relevant to C5 convertases from both classical and alternative pathways. Next, we imaged MAC formation starting from purified soluble C5b6, C7, C8, and C9. Addition of C7 to premixed C5b6, C8, and C9 yielded liposomal leakage with a reduced (<1 min) lag phase because of the absence of antibody binding and the proteolytic cascade of complement activation (Figure S1A). In agreement with this, pre-incubation of liposomes with antibodies reduced the lag phase to 2 min for NHS (Figure S1A). Phase-plate cryo-ET clearly showed isolated pore structures in the liposomal membrane (Figure 1D).

Measuring release of glucose-6-phosphate dehydrogenase (Yamamoto et al., 1995) indicated no leakage from liposomes upon addition of C5b6, C7, and C8 (Figure S1A), whereas we

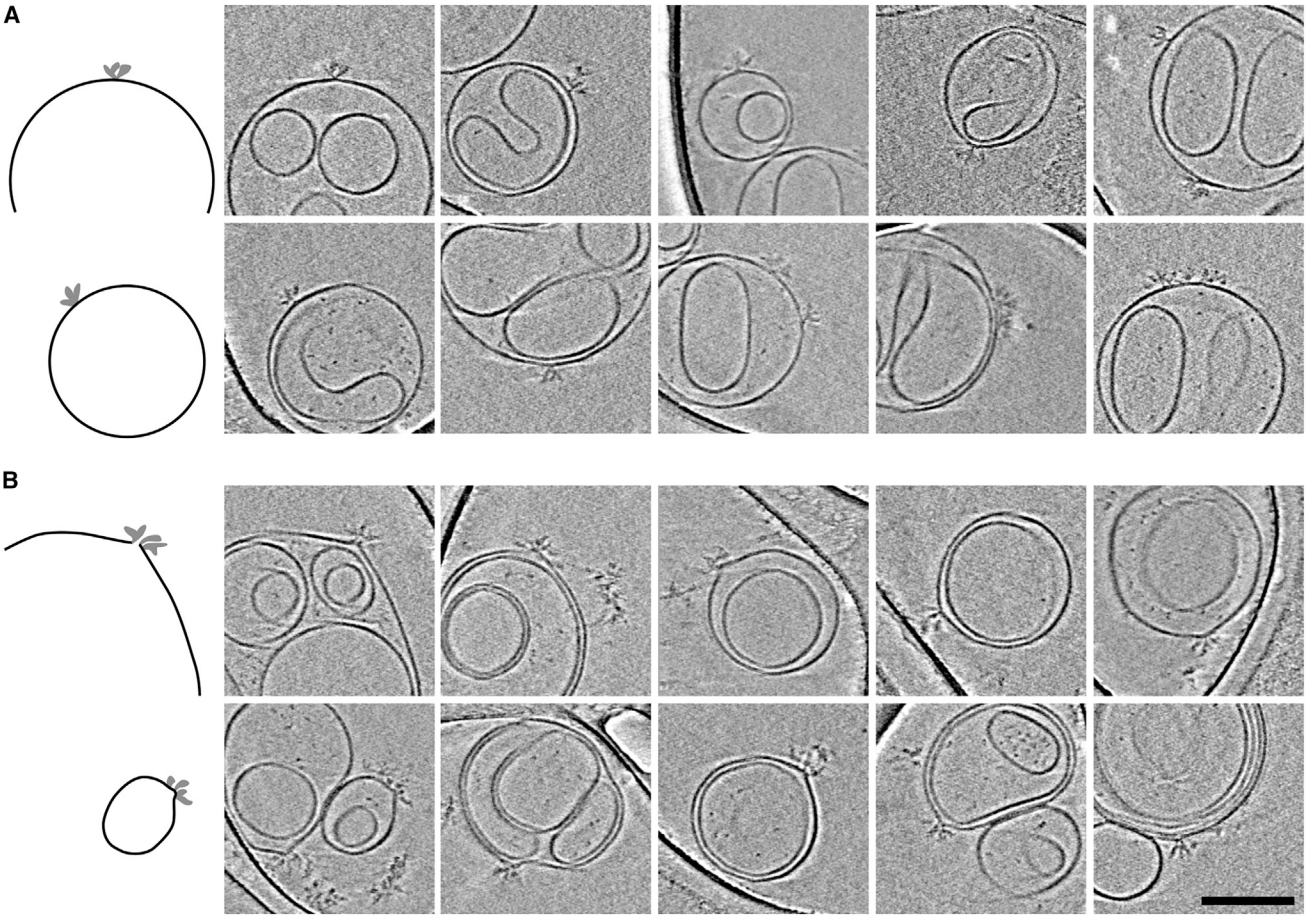

Figure 2. C5b-7 and C5b-8 Bind to and Deform the Membrane, Respectively

(A) Tomographic slices through C5b-7 complexes bound to multilamellar liposome membranes.

(B) Tomographic slices through C5b-8 complexes bound to and deforming liposome membranes.

The first image in each row is a schematic showing the lipid bilayer (black) and protein (gray). Scale bar represents 100 nm.

observed release of sulforhodamine B (Figure S1C). Based on the diameter of the fluorophore versus enzyme, these data indicate a hole size between 1.5 and 7 nm, consistent with earlier reports (Ramm et al., 1982; Zalman and Müller-Eberhard, 1990) that C5b-8, but not C5b-7, makes 3-nm holes in membranes. Phase-plate tomograms of C5b-7 and C5b-8 bound to liposomes indicate spots with one to several plume structures on the membrane surface, with three to four plumes occurring most often (Figure 2). Given the size of the C5b6 complex (22 nm in length; Aleshin et al., 2012a; Hadders et al., 2012), each plume corresponds to one C5b-7 or C5b-8 complex, in agreement with negative-stain electron microscopy reports (DiScipio et al., 1988; Preissner et al., 1985; Tschopp, 1984). The effects on the membrane differ for C5b-7 and C5b-8. At sites of C5b-7 binding, the local curvature of the membrane is unperturbed, as seen on the inner-leaflet side (Figure 2A), which is consistent with the absence of leakage. However, formation of C5b-8 complexes induces protrusion and perforation of the membrane (Figure 2B). Though obscured by the missing wedge effects, three to four C5b-8 complexes form complexes that perforate the membrane, yielding a hole of ~3.5 nm (Figure 2B), in line with previously reported sizes (Ramm et al., 1982; Zalman and Müller-Eberhard, 1990).

A large variation of MAC pores formed in DMPC:DMPG:cholesterol liposomes was observed upon addition of purified components C5b6, C7, C8, and C9. Figure 3 presents the variation in C5b-9 MAC pores on these liposomes observed by cryo-ET, based on data from 73 tomograms using the Volta phase plate and reconstructed using the software-program IMOD (Kremer et al., 1996; Mastronarde, 1997). Pores were de-noised to aid presentation using non-linear anisotropic diffusion (NAD; Frangakis and Hegerl, 2001). Roughly half (518/986) of the occurrences are single C5b-9 ring structures (Figures 3A and 3C), characterized by the presence of a single protrusion at the rim (identifying the C5b678 initiator structure) and a single closed pore (presumably formed by multiple copies of C9). However, more complex arrangements are apparent with pores containing a variable number (two to four) of C5b-8 initiator complexes, which we term composite pores, with various C5b-8 to C5b-8 arrangements possible (Figures 3B and 3D). In some instances, the C5b-8 component is located within the lumen of the pore (e.g., numbers 1–4 in Figure 3B and double arrows in Figures

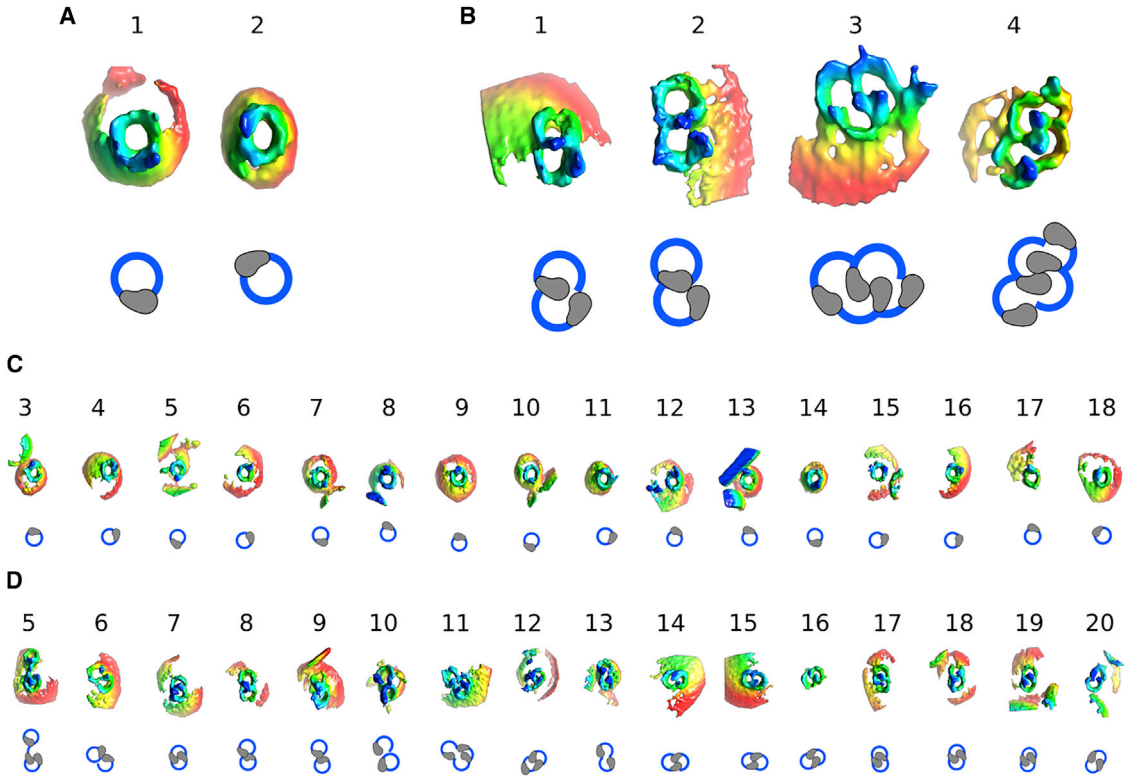

Figure 3. Oligomeric Heterogeneity in MAC Pores

(A) Representative single pores.

(B) Representative multimeric pores.

(C) Overview of single pores.

(D) Overview of multimeric pores.

Subtomograms were de-noised using NAD and colored by height from red (bottom) to blue (top). We interpret C5b-8 based on the height in the tomogram. A schematic is shown below each pore; C5b678 is shown as gray, and C9 rings are shown as blue arcs.

1B and 1C), suggesting that it is fully surrounded by the aqueous solution and not in contact with lipids. C5b-8 components are concatenated with a C9 arc of variable length, suggesting unidirectional growth (though it is not possible to assign C5b-8 unambiguously in every case). A variation of closures is observed, with C9 touching at various sites of C5b-8 and C9 arcs. Similar composite pores are present in experiments with NHS and FB-depleted serum (double arrowheads in Figures 1B and 1C), demonstrating that joined pores are not artifacts from pore formation using purified proteins but rather form upon classical-pathway activation and alternative-pathway amplification. Except for a single instance of an arc connecting two pores (number 5 in Figure 3D), no isolated, non-closed pores were observed in the liposome membranes. However, the composite and single pores observed in these liposomes display similar widths, and formation of extended, joined pores may have a limited effect on sizes of molecules that may leak.

Next, we performed subtomogram averaging after particle picking from 73 tomograms, resulting in 986 subvolumes used for refinement in EMAN2 (Galaz-Montoya et al., 2015; Tang et al., 2007). Subtomogram averaging converged to yield a density map with a resolution of 2.3 nm (Fourier shell correlation [FSC] = 0.143; Figures 4A and S2). ResMap (Kucukelbir et al., 2014) showed highest resolution (1.8–2.6 nm) around the pore ring and protrusion, whereas the lowest resolution was found in the lipid bilayer (likely due to variations in liposome diameter and fluidity of the membrane) and at the top of the protrusion (Figure S2B). The pore shape is clear in the subtomogram-average density map (Figure 4), with a total height of 25 nm and inner and outer diameters of 10 and 25 nm, respectively (Figures S2C and S2D). The large extension above the ring fits with the C5b6 heterodimer previously described (Aleshin et al., 2012a; Hadders et al., 2012). The lumen is slightly conical, constricting from 11.5 to 10 nm from top to bottom (an 8.6-nm difference in height), resulting in an angle of $\sim 5^{\circ}$ (Figures S2C and S2D). In conjunction with this, the barrel is slightly twisted and skewed, with the thickness of the rim varying from 6.8 to 7.3 nm (Figure S2C). Finally, a striking feature of the map is a fissure in the barrel above the membrane (Figure 4D) marking the beginning and the end of the C5b-9 pore structure.

Crystal structures were fitted into the subtomogram-average density map using rigid-body docking with UCSF Chimera (Figures 4B–4F and S3; Pettersen et al., 2004). C5b with C6 complement-control protein (CCP) domains 1 and 2, as found in the C5b6 crystal structures (Aleshin et al., 2012a; Hadders et al., 2012) fitted well into the protrusion on top of the ring (Figure 4).

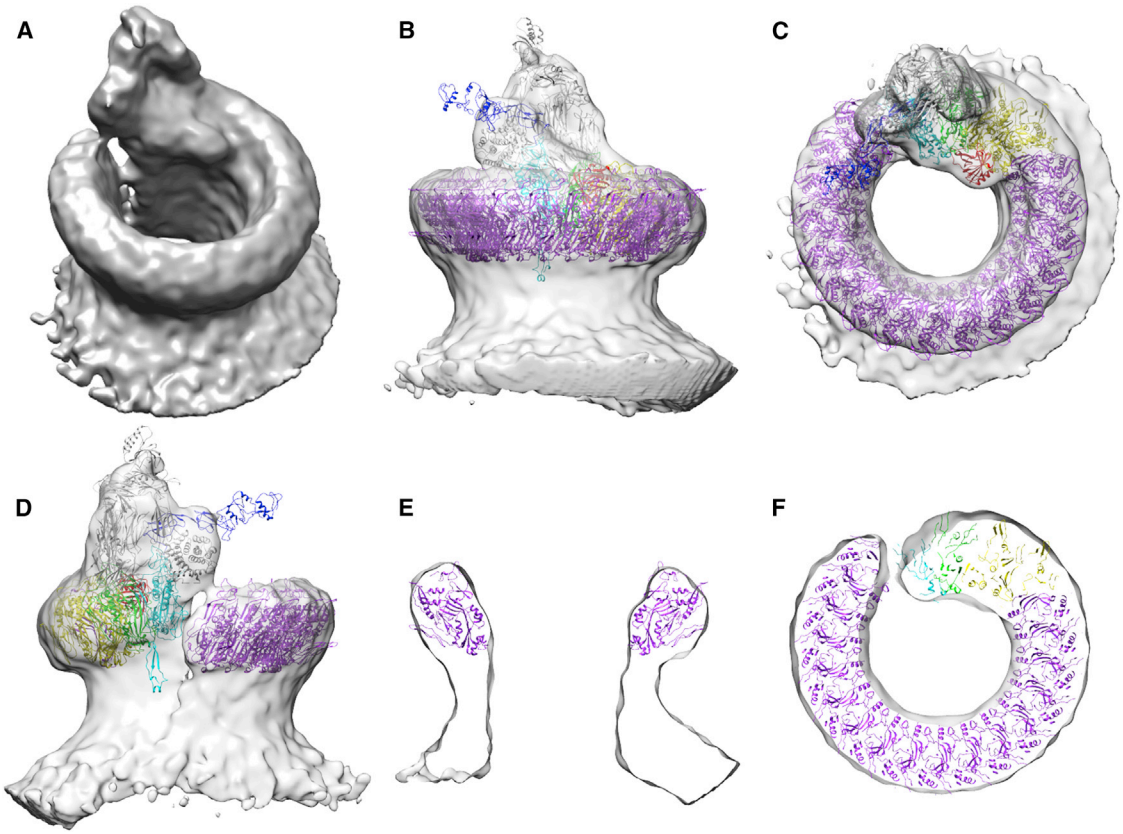

Figure 4. Electron Microscopy Density Map and Fitted Crystal Structures of the MAC Pore

(A) Subtomogram average.

(B and C) Fitted crystal structures. Colors represent C5b (white), C6 TS1-3 domains (cyan), CCP-FIM domains (blue), C7 TS1-2 domains (green), C8αβ domains (yellow), C8γ domains (red), C9 ring (purple), and lipid bilayer (dark gray).

(D) Detail of the C6/9 seam.

(E and F) Orthogonal slices through the density map.

The two C-terminally connected factor I-MAC (FIM) domains of C6 were not resolved in the map (Figures 4 and S4); in the C5b6 crystal structures (Aleshin et al., 2012a; Hadders et al., 2012), these domains are kept in place primarily by crystal contacts. The remaining six domains of C6, thrombospondin (TS) 1 and 2, low-density lipoprotein receptor-like (LR), MACPF, epidermal growth factor like (EGF), and TS3 domains, are part of the β-barrel and rim. For modeling of the rim, we used the structure C6 TS1-TS2-LR-MACPF-EGF-TS3 (Hadders et al., 2012); for C7, we used a copy of C6 minus the first TS1 domain (forming C7 TS1-LR-MACPF-EGF-TS2); C8β and C8α-γ were taken from the crystal structure (Lovelace et al., 2011); and for C9, we used a copy of C8β minus the last TS domain (forming C9 TS1-LR-MACPF-EGF). We generated a ring of C9 copies, with the central kinked β sheet on the inside, to estimate the number of protomers in the ring. The width of the ring corresponds to approximately 22 protomers; however, the density accounts for 20 copies, with 2 copies missing due to the presence of the seam (Figure 4F). Thus, we conclude the ring contains 4 protomer units from C5b6, C7, C8β, and C8α, likely with 16 copies of C9. Clear density inside the pore was visible for C8γ (Figure 4C), which confirms the position of the disulfide bonded C8α; the observation of C8γ on the inside of the pore is in agreement with MACPF orientations in modeling of CDCs (Dang et al., 2005; Tilley et al., 2005), but it contradicts the modeling of perforin (Law et al., 2010). A small region of density is not accounted for in the model, which lies above C7 and between C5b and C8γ, as indicated in Figures S4C and S4D. This density possibly accommodates part of the C7 C-terminal domains CCP1-CCP2-FIM1-FIM2. Moreover, modeling of the protomer units in the slightly helical rim and barrel cannot be performed unambiguously at the given resolution of ~2 nm. In this model, we did not account for the variation in rim thickness (Figure 4E), indicating possible conformational adjustments of C6-7-8β-8α and C9 molecules in the ring. Overall, the C5b678βαγ9_{16} modeling explains the dominant features of the C5b protrusion, the rim made by MACPF and surrounding domains, the pore wall formed by extension of the transmembrane β-hairpins into a large β-barrel (consisting of 20 × 4 β strands), and a seam, indicating a weak closure between terminal C9 and C6 of the C5b-8 MAC initiator.

Conclusions

Using vitrified liposomes, we visualized the heterogeneous structures of MAC initiating C5b-7 and C5b-8 complexes and C5b-9

MAC pores on and in the membrane bilayer. These in situ studies were facilitated by the use of a Volta phase plate mounted on a Titan Krios transmission electron microscope with a Falcon II direct electron detector, enabling identification of the individual complexes and evaluation of the structural heterogeneities using in-focus cryo-ET without the need for labeling or negative staining. Under the experimental conditions used, we observed clustering of the initiating C5b-7 complexes on the membrane, without disturbance of the lipid bilayer; membrane protrusion and hole formation upon oligomerization of C5b-8 complexes; and single and composite pores formed in the membrane bilayer by C5b-9 complexes. Subsequent subtomogram averaging of 740 C5b-9 pores yielded a 2.3-nm resolution map of the MAC pore.

The density map of a subtomogram-averaged single MAC pore revealed an irregular twisted barrel, consistent with C5b6-7-8β-8αγ and likely 16 copies of C9, yielding a slightly conical pore with a seam of weaker density between the last C9 and the C5b-8 complex. All MACPF proteins (i.e., C6, C7, C8β, C8α, and C9) are part of the single-barrel pore. The β-hairpin regions, which are thought to form the transmembrane β-barrel (Shatursky et al., 1999; Shepard et al., 1998), are notably shorter for C6, C7, and to a lesser extent, C8 (Figure S4A). As indicated previously (Aleshin et al., 2012b), the shorter β strands likely explain that C5b-7 complexes merely bind to membranes while C5b-8 perforates the membrane, but full C5b-9 is required to generate the 10-nm pores. With C5b6-7-8β-8α being part of the C5b-9 pore, the shorter β strands of C6, C7, and C8β would imply incomplete membrane-pore formation. The in situ C5b-9 single pore structure indicates that the barrel is narrowed in the membrane. Tightening of the pore in the membrane suggests that the "missing" β strands are accommodated for by making a smaller β-barrel. An apparent consequence of this arrangement is a twisting of the barrel and loss of interactions between the end of C9 and the start of C5b-8, yielding a pronounced seam in the barrel above the membrane.

In conclusion, our data highlight the structural heterogeneity in the MAC-pore formation process. Most recently, two reports presented single-particle cryo-electron microscopy reconstructions of detergent-solubilized poly-C9 (Dudkina et al., 2016) and C5b-9 (Serna et al., 2016). These results are consistent with the main in situ pore features presented here, but the structures either are regular untwisted or show a relaxed twist; this is likely due to using C9 exclusively in the former case and non-native detergent solubilization in the latter. Moreover, these data do not show the extensive structural heterogeneities observed in situ. This diversity possibly serves the mammalian immune system to form MAC structures on various membrane surfaces. Clearly, the complexity of the microbial membranes by far exceeds the simplicity of the liposomes used in these studies. Conceivably, membrane fluidity, protective glycan layers, etc., will affect the formation rates of C5 convertases, initiating MAC formation, and affect multimerization and fusion of MAC, initiating complexes and final pore structures.

EXPERIMENTAL PROCEDURES

Complement Activity Assays

Purified C5b6, C7, C8, and C9 proteins; NHS; and FB-depleted sera were purchased from Complement Technologies and stored at −80°C. Liposomes composed of DMPC:DMPG:cholesterol (45:5:50 mol %; Avanti Polar Lipids) were formed by hydration and extruded to a diameter of 200 nm, as described in Supplemental Information.

For fluorescence assays, 50 mM sulforhodamine B was encapsulated during hydration. Fluorescence was monitored using an excitation wavelength of 565 nm and emission wavelength of 585 nm. Purified C5b6, C7, C8, and C9 proteins were added to liposomes at final concentrations of 25, 25, 25, and 300 nM, respectively; C7 was always added last to initiate pore formation.

For absorbance assays, DNP-labeled liposomes (Wako Diagnostics) were monitored at 340 nm using an Ultrospec 2100 pro (Biochrom), as described (Yamamoto et al., 1995). Sera were used at a final concentration of 2.5 vol %. Purified C5b6, C7, C8, and C9 proteins were used at final concentrations of 15, 15, 15, and 180 nM, respectively; C7 was always added last to initiate pore formation.

Cryo-electron Tomography

Liposomes were mixed with sera or protein and frozen as described in Supplemental Information. Grids were loaded into a Titan Krios transmission electron microscope (FEI Company) equipped with a field emission gun operating at 300 kV and a Volta phase plate (FEI) heated to 225°C and were imaged using a Falcon II direct electron detector (FEI). Before each tilt series, the Volta phase plate was advanced to a new area, allowed to settle for 300 s, and then conditioned for 300 s with a dose of 0.17 nA for a final charge of ~50 nC to generate an approximate phase shift of 90° (Danev et al., 2014). The phase plate was also conditioned for an additional 10 s between each tilt image.

Tilt series were collected in batch mode using the software program Tomography 4.0 (FEI) at ×29,000 magnification, using a discontinuous tilt scheme from 0° to −60° before collecting 0° to +60°, in 2° increments. Total dose for the tilt series was 6,100 e^-/nm^2. Focusing to −500 nm was performed before each image acquisition using a low-dose routine.

Tomogram Reconstruction and Subtomogram Averaging

Tomograms were reconstructed with the software program IMOD (Kremer et al., 1996; Mastronarde, 1997), as described in Supplemental Information. Subtomogram averaging was performed using EMAN2 (Galaz-Montoya et al., 2015) by refining against two independent initial models following gold-standard procedures (Henderson et al., 2012), as detailed in Supplemental Information. Resolution was estimated by applying a tight mask that was independently and automatically generated for the even and odd half-datasets. Resolutions reported are at FSC = 0.143. The electron microscopy density map and associated mask and FSC curve were deposited in the Electron Microscopy Data Bank (http://www.emdatabank.org/) with accession number EMD-3289. The software program ResMap was used to calculate local resolution variations (Kucukelbir et al., 2014).

Model Fitting

Models for C5b6, C7, C8, and C9 were generated as described in Supplemental Information. These were manually positioned in the electron microscopy map using UCSF Chimera (Pettersen et al., 2004) and, due to the limited resolution, refined only by rigid-body fitting (using the function "fit-in-map" of Chimera), as described in Supplemental Information.

ACCESSION NUMBERS

The accession number for the electron microscopy map reported in this paper is EMDB: EMD-3289.

SUPPLEMENTAL INFORMATION

Supplemental Information includes Supplemental Experimental Procedures and four figures and can be found with this article online at http://dx.doi.org/10.1016/j.celrep.2016.03.002.

AUTHOR CONTRIBUTIONS

T.H.S. prepared and conducted liposome assays, cryo-ET experiments, data and image analysis, image reconstruction, and subtomogram averaging.

T.H.S., A.J.K., and P.G. designed the research. T.H.S. and P.G. performed the modeling and wrote the paper.

ACKNOWLEDGMENTS

This work was supported by the Council for Chemical Sciences (CW) of the Netherlands Organization for Scientific Research (NWO grant 700.57.010) and the Netherlands Centre for Electron Nanoscopy (NeCEN), Leiden (NWO grant 175.010.2009.001). We thank Frank Faas for computational and software support, David Mastronarde for advice with IMOD, Jesus Galaz-Montoya and Steve Ludtke for help with EMAN2, and Suzan Rooijakkers for critical reading of the manuscript.

Received: January 19, 2016
Revised: February 9, 2016
Accepted: February 24, 2016
Published: March 24, 2016

REFERENCES

Aleshin, A.E., DiScipio, R.G., Stec, B., and Liddington, R.C. (2012a). Crystal structure of C5b-6 suggests structural basis for priming assembly of the membrane attack complex. J. Biol. Chem. *287*, 19642–19652.

Aleshin, A.E., Schraufstatter, I.U., Stec, B., Bankston, L.A., Liddington, R.C., and DiScipio, R.G. (2012b). Structure of complement C6 suggests a mechanism for initiation and unidirectional, sequential assembly of membrane attack complex (MAC). J. Biol. Chem. *287*, 10210–10222.

Asano, S., Fukuda, Y., Beck, F., Aufderheide, A., Förster, F., Danev, R., and Baumeister, W. (2015). Proteasomes. A molecular census of 26S proteasomes in intact neurons. Science *347*, 439–442.

Asano, S., Engel, B.D., and Baumeister, W. (2016). In situ cryo-electron tomography: a post-reductionist approach to structural biology. J. Mol. Biol. *428* (*2 Pt A*), 332–343.

Bhakdi, S., and Tranum-Jensen, J. (1984). On the cause and nature of C9-related heterogeneity of terminal complement complexes generated on target erythrocytes through the action of whole serum. J. Immunol. *133*, 1453–1463.

Briggs, J.A. (2013). Structural biology in situ—the potential of subtomogram averaging. Curr. Opin. Struct. Biol. *23*, 261–267.

Cooper, N.R., and Müller-Eberhard, H.J. (1970). The reaction mechanism of human C5 in immune hemolysis. J. Exp. Med. *132*, 775–793.

Danev, R., Buijsse, B., Khoshouei, M., Plitzko, J.M., and Baumeister, W. (2014). Volta potential phase plate for in-focus phase contrast transmission electron microscopy. Proc. Natl. Acad. Sci. USA *111*, 15635–15640.

Dang, T.X., Hotze, E.M., Rouiller, I., Tweten, R.K., and Wilson-Kubalek, E.M. (2005). Prepore to pore transition of a cholesterol-dependent cytolysin visualized by electron microscopy. J. Struct. Biol. *150*, 100–108.

DiScipio, R.G., Chakravarti, D.N., Muller-Eberhard, H.J., and Fey, G.H. (1988). The structure of human complement component C7 and the C5b-7 complex. J. Biol. Chem. *263*, 549–560.

Dudkina, N.V., Spicer, B.A., Reboul, C.F., Conroy, P.J., Lukoyanova, N., Elmlund, H., Law, R.H., Ekkel, S.M., Kondos, S.C., Goode, R.J., et al. (2016). Structure of the poly-C9 component of the complement membrane attack complex. Nat. Commun. *7*, 10588.

Frangakis, A.S., and Hegerl, R. (2001). Noise reduction in electron tomographic reconstructions using nonlinear anisotropic diffusion. J. Struct. Biol. *135*, 239–250.

Fredslund, F., Laursen, N.S., Roversi, P., Jenner, L., Oliveira, C.L., Pedersen, J.S., Nunn, M.A., Lea, S.M., Discipio, R., Sottrup-Jensen, L., and Andersen, G.R. (2008). Structure of and influence of a tick complement inhibitor on human complement component 5. Nat. Immunol. *9*, 753–760.

Fukuda, Y., Laugks, U., Lučić, V., Baumeister, W., and Danev, R. (2015). Electron cryotomography of vitrified cells with a Volta phase plate. J. Struct. Biol. *190*, 143–154.

Galaz-Montoya, J.G., Flanagan, J., Schmid, M.F., and Ludtke, S.J. (2015). Single particle tomography in EMAN2. J. Struct. Biol. *190*, 279–290.

Hadders, M.A., Beringer, D.X., and Gros, P. (2007). Structure of C8alpha-MACPF reveals mechanism of membrane attack in complement immune defense. Science *317*, 1552–1554.

Hadders, M.A., Bubeck, D., Roversi, P., Hakobyan, S., Forneris, F., Morgan, B.P., Pangburn, M.K., Llorca, O., Lea, S.M., and Gros, P. (2012). Assembly and regulation of the membrane attack complex based on structures of C5b6 and sC5b9. Cell Rep. *1*, 200–207.

Henderson, R., Sali, A., Baker, M.L., Carragher, B., Devkota, B., Downing, K.H., Egelman, E.H., Feng, Z., Frank, J., Grigorieff, N., et al. (2012). Outcome of the first electron microscopy validation task force meeting. Structure *20*, 205–214.

Hotze, E.M., Wilson-Kubalek, E.M., Rossjohn, J., Parker, M.W., Johnson, A.E., and Tweten, R.K. (2001). Arresting pore formation of a cholesterol-dependent cytolysin by disulfide trapping synchronizes the insertion of the transmembrane beta-sheet from a prepore intermediate. J. Biol. Chem. *276*, 8261–8268.

Kremer, J.R., Mastronarde, D.N., and McIntosh, J.R. (1996). Computer visualization of three-dimensional image data using IMOD. J. Struct. Biol. *116*, 71–76.

Kucukelbir, A., Sigworth, F.J., and Tagare, H.D. (2014). Quantifying the local resolution of cryo-EM density maps. Nat. Methods *11*, 63–65.

Law, R.H., Lukoyanova, N., Voskoboinik, I., Caradoc-Davies, T.T., Baran, K., Dunstone, M.A., D'Angelo, M.E., Orlova, E.V., Coulibaly, F., Verschoor, S., et al. (2010). The structural basis for membrane binding and pore formation by lymphocyte perforin. Nature *468*, 447–451.

Leung, C., Dudkina, N.V., Lukoyanova, N., Hodel, A.W., Farabella, I., Pandurangan, A.P., Jahan, N., Pires Damaso, M., Osmanović, D., Reboul, C.F., et al. (2014). Stepwise visualization of membrane pore formation by suilysin, a bacterial cholesterol-dependent cytolysin. eLife *3*, e04247.

Lovelace, L.L., Cooper, C.L., Sodetz, J.M., and Lebioda, L. (2011). Structure of human C8 protein provides mechanistic insight into membrane pore formation by complement. J. Biol. Chem. *286*, 17585–17592.

Mastronarde, D.N. (1997). Dual-axis tomography: an approach with alignment methods that preserve resolution. J. Struct. Biol. *120*, 343–352.

Morgan, B.P., and Harris, C.L. (2015). Complement, a target for therapy in inflammatory and degenerative diseases. Nat. Rev. Drug Discov. *14*, 857–877.

Müller-Eberhard, H.J. (1986). The membrane attack complex of complement. Annu. Rev. Immunol. *4*, 503–528.

Nogales, E., and Scheres, S.H. (2015). Cryo-EM: a unique tool for the visualization of macromolecular complexity. Mol. Cell *58*, 677–689.

Noris, M., and Remuzzi, G. (2009). Atypical hemolytic-uremic syndrome. N. Engl. J. Med. *361*, 1676–1687.

Parker, C.J. (2007). The pathophysiology of paroxysmal nocturnal hemoglobinuria. Exp. Hematol. *35*, 523–533.

Pettersen, E.F., Goddard, T.D., Huang, C.C., Couch, G.S., Greenblatt, D.M., Meng, E.C., and Ferrin, T.E. (2004). UCSF Chimera—a visualization system for exploratory research and analysis. J. Comput. Chem. *25*, 1605–1612.

Podack, E.R., Tschoop, J., and Müller-Eberhard, H.J. (1982). Molecular organization of C9 within the membrane attack complex of complement. Induction of circular C9 polymerization by the C5b-8 assembly. J. Exp. Med. *156*, 268–282.

Preissner, K.T., Podack, E.R., and Müller-Eberhard, H.J. (1985). The membrane attack complex of complement: relation of C7 to the metastable membrane binding site of the intermediate complex C5b-7. J. Immunol. *135*, 445–451.

Ramm, L.E., Whitlow, M.B., and Mayer, M.M. (1982). Size of the transmembrane channels produced by complement proteins C5b-8. J. Immunol. *129*, 1143–1146.

Ricklin, D., Hajishengallis, G., Yang, K., and Lambris, J.D. (2010). Complement: a key system for immune surveillance and homeostasis. Nat. Immunol. *11*, 785–797.

Rosado, C.J., Buckle, A.M., Law, R.H., Butcher, R.E., Kan, W.T., Bird, C.H., Ung, K., Browne, K.A., Baran, K., Bashtannyk-Puhalovich, T.A., et al. (2007). A common fold mediates vertebrate defense and bacterial attack. Science *317*, 1548–1551.

Serna, M., Giles, J.L., Morgan, B.P., and Bubeck, D. (2016). Structural basis of complement membrane attack complex formation. Nat. Commun. *7*, 10587.

Shatursky, O., Heuck, A.P., Shepard, L.A., Rossjohn, J., Parker, M.W., Johnson, A.E., and Tweten, R.K. (1999). The mechanism of membrane insertion for a cholesterol-dependent cytolysin: a novel paradigm for pore-forming toxins. Cell *99*, 293–299.

Shepard, L.A., Heuck, A.P., Hamman, B.D., Rossjohn, J., Parker, M.W., Ryan, K.R., Johnson, A.E., and Tweten, R.K. (1998). Identification of a membrane-spanning domain of the thiol-activated pore-forming toxin *Clostridium perfringens* perfringolysin O: an α-helical to beta-sheet transition identified by fluorescence spectroscopy. Biochemistry *37*, 14563–14574.

Sonnen, A.F., Plitzko, J.M., and Gilbert, R.J. (2014). Incomplete pneumolysin oligomers form membrane pores. Open Biol. *4*, 140044.

Stephens, D.S., Greenwood, B., and Brandtzaeg, P. (2007). Epidemic meningitis, meningococcaemia, and *Neisseria meningitidis*. Lancet *369*, 2196–2210.

Tang, G., Peng, L., Baldwin, P.R., Mann, D.S., Jiang, W., Rees, I., and Ludtke, S.J. (2007). EMAN2: an extensible image processing suite for electron microscopy. J. Struct. Biol. *157*, 38–46.

Tilley, S.J., Orlova, E.V., Gilbert, R.J., Andrew, P.W., and Saibil, H.R. (2005). Structural basis of pore formation by the bacterial toxin pneumolysin. Cell *121*, 247–256.

Tschopp, J. (1984). Ultrastructure of the membrane attack complex of complement. Heterogeneity of the complex caused by different degree of C9 polymerization. J. Biol. Chem. *259*, 7857–7863.

Yamamoto, S., Kubotsu, K., Kida, M., Kondo, K., Matsuura, S., Uchiyama, S., Yonekawa, O., and Kanno, T. (1995). Automated homogeneous liposome-based assay system for total complement activity. Clin. Chem. *41*, 586–590.

Zalman, L.S., and Müller-Eberhard, H.J. (1990). Comparison of channels formed by poly C9, C5b-8 and the membrane attack complex of complement. Mol. Immunol. *27*, 533–537.